

Light-shift tomography in an optical-dipole trap for neutral atoms

J. P. Brantut, J. F. Clément, M. Robert de Saint Vincent, G. Varoquaux, R. A. Nyman,^{*} A. Aspect, T. Bourdel, and P. Bouyer
Laboratoire Charles Fabry de l'Institut d'Optique, Univ Paris Sud, CNRS, Campus Polytechnique RD128 91127 Palaiseau, France
 (Received 21 July 2008; published 25 September 2008)

We report on light-shift tomography of a cloud of ^{87}Rb atoms in a far-detuned optical-dipole trap at 1565 nm. Our method is based on standard absorption imaging, but takes advantage of the strong light shift of the excited state of the imaging transition, which is due to a quaresonance of the trapping laser with a higher excited level. We use this method to (i) map the equipotentials of a crossed optical-dipole trap and (ii) study the thermalization of an atomic cloud by following the evolution of the potential energy of atoms during the free-evaporation process.

DOI: 10.1103/PhysRevA.78.031401

PACS number(s): 37.10.Gh, 32.60.+i, 33.40.+f

In situ studies of ultracold atomic gases can yield invaluable information. Imaging on the one hand [1–5] and light-shift spectroscopy on the other hand [6–9] have independently proved successful in the investigations of cold neutral gases. In this paper, we present a light-shift tomography method combining *in situ* absorption imaging and light-shift spectroscopy to yield an image, and/or the number, of atoms at a given potential energy in an optical-dipole trap. It takes advantage of the strong light shifts of the upper $5P_{3/2}$ level of the imaging transition of ^{87}Rb under the influence of our trapping laser at 1565 nm. This is due to quaresonances to higher excited states ($4D_{3/2}$ and $4D_{5/2}$) at 1529 nm. As a consequence, although the light shift experienced by atoms in the ground state ($5S_{1/2}$)—i.e., the trapping potential—is moderate, the shift of the imaging transition can be large compared to its natural linewidth. It thus allows us to perform spectrally resolved imaging of the atomic cloud.

We use this technique for two different goals: (i) *Mapping of the optical potential*. Starting with a cold cloud with a smooth density profile, we suddenly switch on a trapping laser at 1565 nm and immediately take an absorption image of the atoms in the presence of the trap, before any evolution of the atomic density. By repeating this imaging at various probe-laser frequencies, we obtain a map of the equal light-shift regions; i.e., we perform tomography of the trap potential [10]. (ii) *Measurement of the atomic potential-energy distribution*. Counting the number of atoms at a given probe detuning—i.e., at a given potential energy in the trap—and repeating this measurement at various probe detunings, we directly measure the potential-energy distribution of the cloud. This allows us to study the relaxation of a trapped atomic cloud from an initial out-of-equilibrium situation towards a thermal distribution by monitoring the evolution of the potential-energy distribution during the free-evaporation process [11].

As shown in Fig. 1(a), we image ^{87}Rb atoms using a probe resonant with the $5S_{1/2}$ ($F=2$) to $5P_{3/2}$ ($F'=3$) transition at 780 nm (D_2), perturbed by the trapping laser at 1565 nm. In order to evaluate the light shifts of the ground and excited states of the D_2 imaging transition, we have computed the polarizabilities (α_g and α_e , respectively) of

these states for the 1565-nm laser excitation. The transitions giving the main contributions are shown in Fig. 1(a). The moderate detuning of the trapping laser with respect to the $5P$ to $4D$ transitions, compared to the $5S$ to $5P$, leads to a polarizability of the $5P_{3/2}$ state greater than that of the ground state by a factor of $\frac{\alpha_e}{\alpha_g} = 42.6$.

As the light shifts of the energy levels are all proportional to the trapping-laser intensity, the light shift of the ground state—i.e., the potential energy of an atom in the trap E_p (neglecting gravity)—is proportional to the light shift of the imaging transition Δ :

$$\hbar\Delta = \left(\frac{\alpha_e}{\alpha_g} - 1 \right) E_p = 41.6 E_p. \quad (1)$$

As indicated below, we operate in a situation where the ground-state light shift is of a few MHz only, whereas the light shift of the $5P_{3/2}$ level is much larger than the natural linewidth of the probe transition, $\Gamma/2\pi = 6.1$ MHz. In fact, when one considers the various magnetic sublevels of the hyperfine levels $F=2$ and $F'=3$, there is an additional

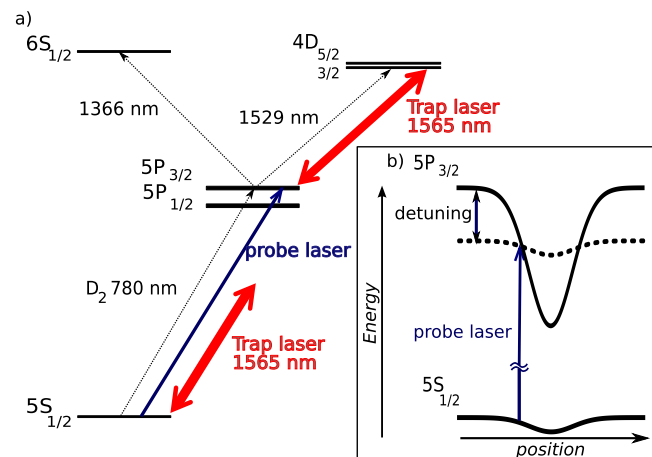


FIG. 1. (Color online) (a) Energy diagram of the lowest energy levels of ^{87}Rb . The strong transitions at 1529 nm are responsible for the 42.6 enhancement factor in light shift of the $5P_{3/2}$ energy level with respect to the $5S_{1/2}$ ground state. (b) Light shifts of the $5S_{1/2}$ and $5P_{3/2}$ levels under the influence of a Gaussian focused laser at 1565 nm (not on scale). The probe laser interacts with atoms at a position which depends on the probe detuning.

^{*}Present address: Centre for Cold Matter, Imperial College, London, SW7 2BW, UK.

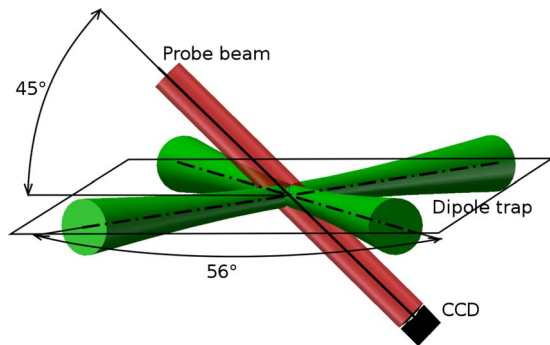


FIG. 2. (Color online) Beam configuration of the dipole trap and the probe.

intensity-dependent broadening, but it remains small compared to the light shift Δ [12,13].

As a consequence, we can spectrally resolve the potential energy of the atoms in the trapping beams. As shown in Fig. 1(b), by taking an *in situ* absorption image with a chosen detuning δ of the probe laser, we detect atoms situated at positions \mathbf{r} such that $U(\mathbf{r}) = \frac{\hbar\delta}{41.6}$, where $U(\mathbf{r})$ is the trapping potential ($U=0$ in free space). We thus directly obtain a map of the trapping potential $U(\mathbf{r})$. The potential-energy resolution is equal to the linewidth of the imaging transition divided by 41.6, according to Eq. (1) (corresponding to 0.14 MHz or $7 \mu\text{K} \times k_B$).

The experimental setup is as follows: in a first vacuum chamber, ^{87}Rb atoms are collected from an atomic vapor created by a dispenser in a two-dimensional magneto-optical trap (2D MOT). Atoms are then transferred into a second chamber where they are trapped in a 3D MOT. The laser system for 2D and 3D MOTs is based on tapered-amplified extended-cavity diode lasers, as described in [14]. The probe beam is generated by a dedicated, offset-locked laser, which can be detuned by 350 MHz from the $F=2$ to $F'=3$ transition and is linearly polarized.

The dipole-trap light is generated by a 50-W erbium-doped fiber laser at 1565 nm (IPG ELR-50). This laser is focused to a $50\text{-}\mu\text{m}$ waist onto the atomic cloud through a lens that can be moved along the optical axis via a motorized translation stage (Aerotech ANT-50L), allowing us to adjust the beam diameter at the atomic position (much as in Ref. [15]). Light is then refocused onto the atoms by a 1:1 telescope to create a crossed-beam configuration, with a crossing angle of 56° , and linear orthogonal polarizations. The beam configuration is shown in Fig. 2. Throughout this paper, the movable lens is adjusted such that at the dipole trap crossing, the beam diameters are about $200 \mu\text{m}$. The optical power is controlled at the output of the laser by an electro-optic modulator and a Glan polarizer. The angle of incidence of the trapping beams with respect to the vacuum-chamber window is 28° , leading to astigmatism of the beams. We compensate this effect to first order on the first-pass beam using a tilted, glass plate.

We use light-shift tomography of the optical-dipole trap to map the potential landscape, using atoms as local probes of the potential. About 10^8 ^{87}Rb atoms are collected in the 3D MOT with a magnetic field gradient of 12.5 G cm^{-1} and a

detuning of the cooling laser of 2.5Γ . The 3D MOT is then compressed down to $200 \mu\text{m}$ (rms radius) by increasing the detuning of the cooling laser up to 10Γ . The cooling beams are switched off, and the dipole trap laser is switched on 1 ms later. After another millisecond an absorption image is taken with a $50\text{-}\mu\text{s}$ pulse at the chosen probe detuning. A repumping laser resonant with the free space $F=1$ to $F'=2$ transition is applied together with the imaging laser. At resonance, atoms scatter about 100 photons during the imaging pulse and the atomic density has no time to evolve.

Examples of absorption images are shown in Fig. 3. At moderate probe detuning (-40 MHz), we see open equipotentials [Fig. 3(a)], which means that we probe atoms which will be able to escape along the directions of the two beams. In this image, we can detect an asymmetry of the trapping potential between the two arms of the dipole trap, which is related to intensity imbalance and residual astigmatism. The decrease of the contrast at the edges of the image is due to the vanishing atomic density. For larger detunings (-80 MHz), the images [Fig. 3(b)] show closed equipotentials with elliptic contours. As we go deeper in the trap (-100 MHz), we reach the bottom, where the equipotentials merge into a spot [Fig. 3(c)].

This tomographic method allows us to determine *in situ* the trap characteristics. The potential landscape at the bottom of the trap yields the trap frequencies (110 ± 10 Hz, 110 ± 10 Hz, and 150 ± 10 Hz), and the detuning at which we observe the change from closed to open equipotentials yields the trap depth ($57 \mu\text{K} \times k_B$ in our experiment). We observe that the shape of the crossed region as probed by tomography is very sensitive to the overlap of the two arms, which provides us with a direct and accurate alignment method [16].

We evaluate the spatial resolution of the potential mapping as follows: in a place where the trapping potential gradient is ∇U , the spatial resolution associated with the linewidth Γ of the probe transition is $d = \frac{\alpha_g}{\alpha_e - \alpha_g} \frac{\hbar\Gamma}{|\nabla U(\mathbf{r})|} \approx 1/41.6 \frac{\hbar\Gamma}{|\nabla U(\mathbf{r})|}$. In our experimental conditions, at the places of steepest gradients, $d = 10 \mu\text{m}$, whereas the resolution of our imaging setup is $7 \mu\text{m}$. The widths of the peaks in the insets of Figs. 3(b) and 3(c) are consistent with the convolution of the two effects. Actually, d could be made smaller than the spatial resolution of the imaging system, either by increasing the light-shift gradients or by using a narrower transition [17,18].

We now turn to the measurement of the potential-energy distribution of the atomic cloud. For each value of the probe detuning—i.e., of the potential energy [Eq. (1)]—we count the number of atoms by integration of the optical density in the corresponding *in situ* absorption image (any spatial information is lost). Repeating this measurement at various values of the detuning, we obtain the atomic potential-energy distribution convolved with our energy-resolution line shape. As in our case the measured atom number varies smoothly at the scale of the resolution ($7 \mu\text{K} \times k_B$), it is simply proportional to the atomic potential-energy distribution.

Using this technique, we follow the evolution of an optically trapped cloud under the effect of free evaporation. Experimentally, we load atoms in a compressed MOT; we then

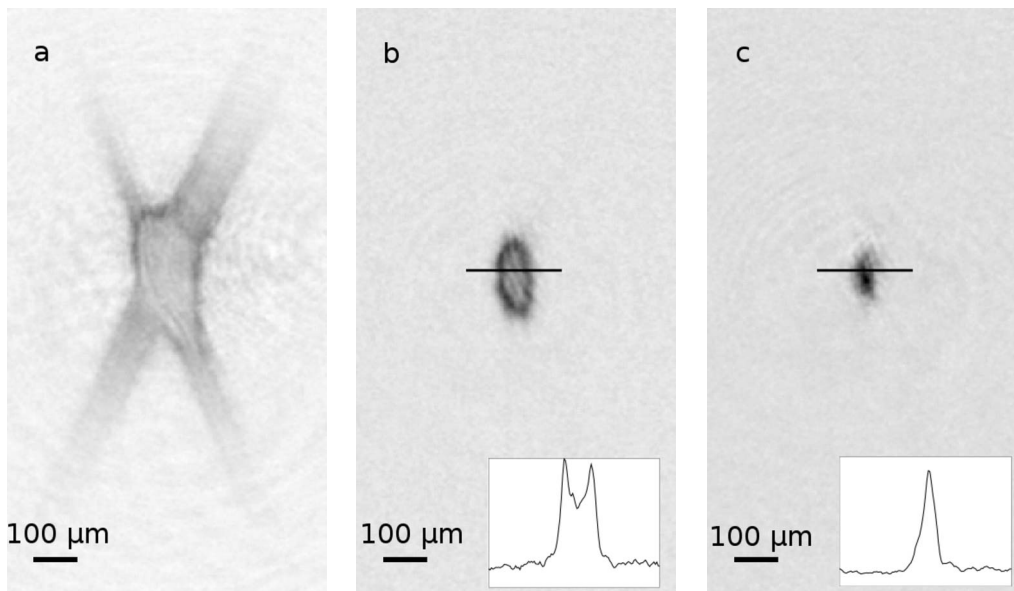


FIG. 3. Absorption images taken 1 ms after switching on the optical-dipole trap, showing the equipotentials of the trap. By choosing the probe laser detuning with respect to the free-space imaging transition [(a) -40 MHz, (b) -80 MHz, and (c) -100 MHz, corresponding to potential energy in the ground state of -45 , -91 , and $-115 \mu\text{K} \times k_B$, respectively] we observe the distribution of equal laser-intensity regions—i.e., equipotentials of the trap. The probe-laser propagation axis is inclined by 45° with respect to the crossed dipole trap plane. Images in the insets of (b) and (c) show cuts along the horizontal axis.

turn off the cooling laser and load the atoms into the dipole trap [19]. We then wait for a given time and image *in situ* the trapped cloud at various detunings.

Figure 4 shows the observed atomic potential-energy distribution after various evolution times, averaged over four images per data point. At short evolution times (<50 ms),

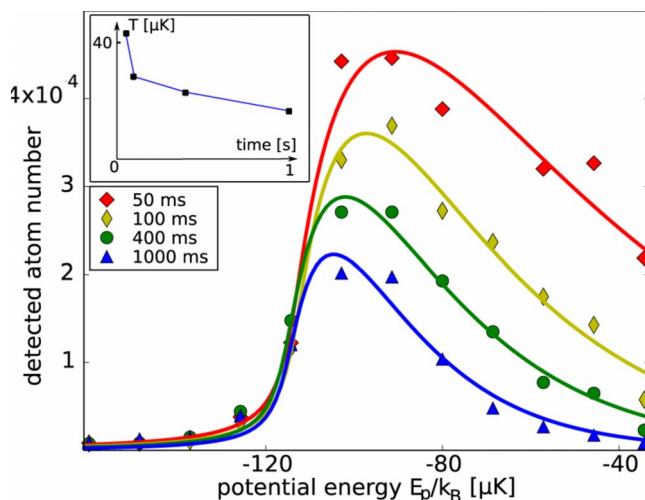


FIG. 4. (Color online) Thermalization of the atomic cloud in the trap (trap bottom is at $E_p/k_B = -115 \mu\text{K}$; equipotentials are closed at $E_p/k_B = -58 \mu\text{K}$). The number of detected atoms in the trap is measured as a function of potential energy after different evolution times. The potential energy is taken to be zero in free space. Solid curves are fits for a thermal gas taking into account the finite linewidth of the imaging transition [using Eq. (2)]. Fitted temperatures are 41, 27, 22, and $16 \mu\text{K}$, consistent with time-of-flight measurements. The inset shows the evolution of the fitted temperature of the cloud as a function of time.

the measurement is blurred by the untrapped atoms falling from the magneto-optical trap. After 50 ms, the atomic distribution extends far into the anharmonic region of the trap, in particular into the two arms where atoms can escape. The fact that we can observe atoms with a potential energy greater than the trap depth is a signature of the nonergodicity of the free-evaporation process: atoms have enough energy to escape, but temporarily remain in the trapping region. Not all the available regions of phase space are explored in the time scale of the experiment [20]. The potential energy at the bottom of the trap is $E_p/k_B = -115 \mu\text{K}$. The nonzero signal at deeper potential energy is due to the finite linewidth of the imaging transition [12].

As the thermalization proceeds, the number of atoms located in regions of high potential energy diminishes faster than the number of atoms at the bottom of the trap. This process results in a lower mean potential energy of the remaining atoms. To characterize our results better, we fit our data with the theoretically predicted atom number $N(\delta)$ at a given probe detuning, in the case of N_{tot} classical atoms at thermal equilibrium in a harmonic trap, taking into account the finite linewidth of the imaging transition:

$$N(\delta) = \frac{4N_{\text{tot}}}{\sqrt{\pi}} \int_0^\infty \frac{u^2 e^{-u^2} du}{1 + 4(\delta + v - tu^2)^2}, \quad (2)$$

where $t = \frac{k_B T}{\hbar \Gamma} \left(\frac{\alpha_c}{\alpha_g} - 1 \right)$, $v = \frac{U(r=0)}{\hbar \Gamma} \frac{\alpha_c}{\alpha_g}$, and $\delta = \frac{\omega - \omega_0}{\Gamma}$ (ω_0 is the unshifted probe-transition frequency) are normalized temperature, minimal potential energy, and detunings, respectively. The fit is unexpectedly good given the fact that the trap is harmonic only close to the bottom. The fitted temperatures are, to within 10% uncertainty, consistent with complemen-

tary measurements of the velocity distribution obtained by the time-of-flight method.

The inset in Fig. 4 shows the evolution of the temperature with the free-evaporation time. We first observe a rapid decrease of the temperature in 100 ms, which we attribute to a simple loss of atoms with an energy larger than the trap depth. It takes a few trap periods for the energetic atoms to find their path to escape along one of the two trapping beams. At longer times, we observe a slower decrease of the temperature, consistent with collision-induced evaporation, as we estimate the initial collision rate in our trap to be of the order of 3 s^{-1} . The lifetime in this experiment is limited to 2 s by background gas collisions, and we nevertheless measure an increase in phase-space density by a factor of 5 between the loaded cloud at 50 ms and the thermal, trapped cloud at equilibrium after 1 s.

In conclusion, we have presented a method to directly map the potential created on ^{87}Rb by an erbium-doped fiber laser at 1565 nm and to directly measure the atomic potential-energy distribution. The energy resolution ($7 \mu\text{K} \times k_B$) could be improved using a trapping wavelength closer to the 1529-nm transition and an appropriate probe polariza-

tion [12]. This method is not specific to ^{87}Rb and could be generalized to other alkali-metal gases which have strong transitions from the $nP_{3/2}$ state to higher excited states in the midinfrared (e.g., Cs at 1469 nm, K at 1252 nm) [21].

The potential-energy resolution of this technique is independent of the spatial resolution of the imaging setup. For a rapidly spatially varying light field, this technique could achieve subwavelength resolution. For example, in a three-dimensional, cubic, optical lattice, the detuned probe laser would be resonant with atoms situated in spherical shells centered on each lattice site, the radii being related to the probe-laser detuning. Light-shift tomography, allowing *in situ* local probing, is likely to be useful in the context of both quantum gas studies and quantum information processing using cold atoms.

We acknowledge technical assistance from F. Moron and A. Villing. This research was supported by CNRS, CNES (as part of the ICE project), ANR (project “blanc” MélaBo-Féria), IFRAF, European Union (through the STREP program FINAQS), and ESA (through the MAP program SAI).

-
- [1] M. R. Andrews, M.-O. Mewes, N. J. van Druten, D. S. Durfee, D. M. Kurn, and W. Ketterle, *Science* **273**, 84 (1996).
- [2] W. Yu-Zhu, Z. Shu-Yu, L. Quan, Z. Shan-Yu, and F. Hai-Xiang, *Chin. Phys. Lett.* **20**, 799 (2003).
- [3] J. M. Higbie *et al.*, *Phys. Rev. Lett.* **95**, 050401 (2005).
- [4] J. Esteve, J.-B. Trebbia, T. Schumm, A. Aspect, C. I. Westbrook, and I. Bouchoule, *Phys. Rev. Lett.* **96**, 130403 (2006).
- [5] T. Gericke, P. Wurtz, D. Reitz, T. Langen, and H. Ott, e-print arXiv:0804.4788.
- [6] C. Salomon, J. Dalibard, A. Aspect, H. Metcalf, and C. Cohen-Tannoudji, *Phys. Rev. Lett.* **59**, 1659 (1987).
- [7] M. Takamoto and H. Katori, *Phys. Rev. Lett.* **91**, 223001 (2003).
- [8] P. F. Griffin, K. J. Weatherill, S. G. MacLeod, R. M. Potvliege, and C. S. Adams, *New J. Phys.* **8**, 11 (2006).
- [9] D. Clément, A. F. Varón, J. A. Retter, L. Sanchez-Palencia, A. Aspect, and P. Bouyer, *New J. Phys.* **8**, 165 (2006).
- [10] P. Courteille, S. Muniz, K. Magalhaes, R. Kaiser, L. Marcassa, and V. Bagnato, *Eur. Phys. J. D* **15**, 173 (2001).
- [11] A. Browaeys, A. Robert, O. Sirjean, J. Poupard, S. Nowak, D. Boiron, C. I. Westbrook, and A. Aspect, *Phys. Rev. A* **64**, 034703 (2001).
- [12] The tensor polarizability leads to a difference in the polarizability of the various magnetic sublevels of the $5P_{3/2}$ ($F'=3$) state of about 20% [13]. Due to the orthogonal polarizations of the two arms of the crossed-dipole trap, the polarization of the trapping laser is ill defined in the trap, and we assume a uniform distribution of the atoms over the various magnetic sublevels of the ground level $5S_{1/2}$ ($F=2$). The broadening of the probe transition is then evaluated by taking equal polarization components for the probe beams. This results in an intensity-dependent broadening that can be as large as 12% of the shift of the transition, which adds to the natural linewidth (6.1 MHz).
- [13] B. Arora, M. S. Safronova, and C. W. Clark, *Phys. Rev. A* **76**, 052509 (2007).
- [14] R. Nyman, G. Varoquaux, B. Villier, D. Sacchet, F. Moron, Y. Le Coq, A. Aspect, and P. Bouyer, *Rev. Sci. Instrum.* **77**, 033105 (2006).
- [15] T. Kinoshita, T. Wenger, and D. S. Weiss, *Phys. Rev. A* **71**, 011602(R) (2005).
- [16] We can evaluate *in situ* the beam quality factor by measuring the maximum light shift at various positions. For our first beam, we measure $M^2=3.5$. We attribute this rather poor value to thermal effects in our electro-optic modulator.
- [17] J. E. Thomas, *Phys. Rev. A* **42**, 5652 (1990).
- [18] J. R. Gardner, M. L. Marable, G. R. Welch, and J. E. Thomas, *Phys. Rev. Lett.* **70**, 3404 (1993).
- [19] The strong redshift of the cycling transition raises specific problems in the loading process from a MOT or an optical molasses. Here we address this problem by rapidly alternating the optical dipole trap and the cooling lasers (10 kHz). Efficient loading of an optical-dipole trap at 1565 nm will be described in a further publication.
- [20] W. Ketterle and N. Van Druten, *Adv. At., Mol., Opt. Phys.* **37**, 181 (1996).
- [21] Yu. Ralchenko, A. E. Kramida, J. Reader, and NIST ASD Team, NIST Atomic Spectra Database (version 3.1.4), NIST, Gaithersburg, MD, 2008.